

First ground-based 200- μm observing with THUMPER on JCMT – sky characterisation and planet maps

D. Ward-Thompson¹, P. A. R. Ade¹, H. Araujo², I. Coulson³, J. Cox¹, G. R. Davis³, Rh. Evans^{1,4}, M. J. Griffin¹, W. K. Gear¹, P. Hargrave¹, P. Hargreaves¹, D. Hayton¹, B. J. Kiernan¹, S. J. Leeks^{1,5}, P. Mauskopf¹, D. Naylor⁶, N. Potter¹, S. A. Rinehart⁷, R. Sudiwala¹, C. R. Tucker¹, R. J. Walker^{1,2}, S. L. Watkin¹

¹ *Department of Physics and Astronomy, Cardiff University, 5 The Parade, Cardiff, CF24 3YB*

² *Blackett Laboratory, Imperial College, London SW7 2BW*

³ *Joint Astronomy Centre, 665 N. A'ohoku Street, Hilo, Hawaii, USA*

⁴ *Glamorgan University, Pontypridd, CF37 1DL*

⁵ *European Space Astronomy Centre, Villafranca del Castillo, PO Box 50727, 28080 Madrid, Spain*

⁶ *Department of Physics, University of Lethbridge, 4401 University Drive, Lethbridge, Alberta, Canada*

⁷ *Laboratory for Astronomy and Solar Physics, Goddard Space Flight Center, Washington D.C., USA*

Accepted 2005 September 1; received 2005 September 1; in original form 2005 July 1.

ABSTRACT

We present observations that were carried out with the Two Hundred Micron Photometer (THUMPER) mounted on the James Clerk Maxwell Telescope (JCMT) in Hawaii, at a wavelength of 200 μm (frequency 1.5 THz). The observations utilise a small atmospheric window that opens up at this wavelength under very dry conditions at high-altitude observing sites. The atmosphere was calibrated using the sky-dipping method and a relation was established between the optical depth, τ , at 1.5 THz and that at 225 GHz: $\tau_{1.5\text{THz}} = (95 \pm 10) \times \tau_{225\text{GHz}}$. Mars and Jupiter were mapped from the ground at this wavelength for the first time, and the system characteristics measured. A noise equivalent flux density (NEFD) of $\sim 65 \pm 10$ Jy (1σ 1s) was measured for the THUMPER–JCMT combination, consistent with predictions based upon our laboratory measurements. The main-beam resolution of 14 arcsec was confirmed and an extended error-beam detected at roughly two-thirds of the magnitude of the main beam. Measurements of the Sun allow us to estimate that the fraction of the power in the main beam is $\sim 15\%$, consistent with predictions based on modelling the dish surface accuracy. It is therefore shown that the sky over Mauna Kea is suitable for astronomy at this wavelength under the best conditions. However, higher or drier sites should have a larger number of useable nights per year.

Key words: instrumentation: photometers – techniques: photometric – infrared: Solar system – submillimetre

1 INTRODUCTION

Far-infrared astronomy is largely the preserve of telescopes borne on satellites, balloons and aircraft. The Infra-Red Astronomical Satellite, IRAS (Beichman et al., 1988) operated at wavelengths as long as 100 μm . The Kuiper Airborne Observatory, KAO (Cameron, Bader & Mobley 1971; Harvey 1979), the Infrared Space Observatory, ISO (Kessler et al., 1996), and the Spitzer Space Telescope (Werner et al., 2004) were designed to operate out to 200 μm . A number of planned missions such as Herschel and Planck aim to cover still longer wavelengths. However, a problem with all such airborne and satellite telescopes is that they are un-

likely to be as large as telescopes that can be built on the ground. Consequently, airborne and orbiting telescopes do not have the angular resolution of comparable ground-based instruments. Therefore, any instruments that can be operated from the ground at these wavelengths and mounted on large telescopes will automatically have a resolution advantage.

Only a limited number of previous ground-based astronomical observations have been made at far-infrared wavelengths. This is because the atmosphere is largely opaque in this regime. However, spectral measurements of the atmosphere, coupled with detailed modelling of atmospheric properties, have shown that there are some small windows

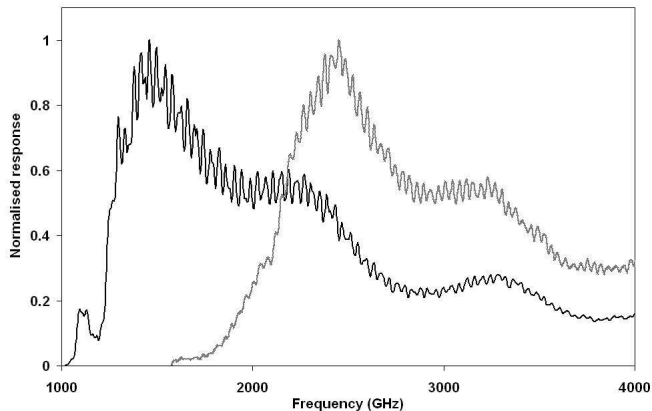


Figure 1. Plot of normalised crystal response versus frequency for an unstressed crystal (lighter line to the right) and a stressed crystal (heavier line to the left) in the THUMPER detector array. Note how the peak response has moved to the required THUMPER frequency of 1500 GHz.

that do open up across this range on very high, dry sites under good conditions. One such window is that at $200\ \mu\text{m}$, corresponding to a frequency of 1.5 THz.

Previous ground-based measurements at this frequency have only been made spectroscopically. No previous ground-based imaging camera has been built to work at this frequency. The spectroscopic observations include Fourier Transform Spectrometer (FTS) measurements at Pampa la Bola in Chile (Matsuo, Sakamoto & Matsushita 1998; Matsushita et al., 1999). These latter authors derived measurements relating the optical depths in different atmospheric pass-bands, including that at $200\ \mu\text{m}$. Ground-based FTS measurements at Mauna Kea in Hawaii have been carried out by a number of groups (e.g. Serabyn & Weisstein 1996; Serabyn et al., 1998; Pardo et al., 2004). All have confirmed the existence of an atmospheric window at $200\ \mu\text{m}$, albeit with varying levels of transmission, depending upon the conditions.

Paine et al., (2000) carried out similar FTS measurements at both Mauna Kea in Hawaii and at Chajnantor in Chile and measured the atmospheric transmission from about 300 to 3000 GHz. They measured the 1.5-THz window and found significant transmission in the wave-band of interest at both locations. Other work at this frequency has included plans for a heterodyne system to operate at the South Pole by a group who have made FTS sky measurements, broadly confirming the above-mentioned results (Chamberlin et al., 2003; Gerech et al., 2003).

In this paper, we present the results from the first commissioning run of the Two HUNDred Micron Photometer (THUMPER) at the James Clerk Maxwell Telescope (JCMT). This instrument is a prototype camera built at Cardiff University to demonstrate the viability of carrying out high-resolution broad-band imaging at $200\ \mu\text{m}$ from the ground.

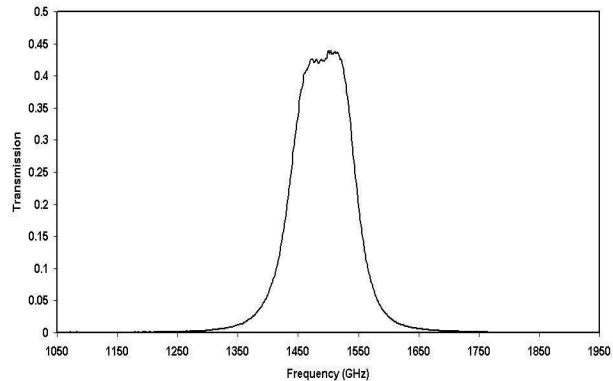


Figure 2. Plot of filter transmission versus frequency for the complete filter stack in THUMPER. The atmospheric central frequency corresponds to 1500 GHz.

2 THE INSTRUMENT

THUMPER consists of a 7-channel array of photoconductor pixel elements arranged on a hexagonal grid (Ward-Thompson et al., 2002; Walker et al., 2003; Evans et al., 2005). This is designed to match the layout of the central pixels in the Sub-millimetre Common User Bolometer Array, SCUBA (Holland et al., 1999), when placed at the Nasmyth focus of the James Clerk Maxwell Telescope (JCMT) on Mauna Kea, Hawaii. This is at an altitude of 4092 m, and is one of the best sites for sub-millimetre observations in the world.

The THUMPER detectors are photo-conductors made from gallium-doped germanium (in the ratio Ge:Ga $\sim 10^5:1$) crystal semi-conductors, which have been stressed to move their peak responsivities into the $200\text{-}\mu\text{m}$ waveband (Walker et al., 2003; Walker 2004). Figure 1 shows a typical crystal responsivity as a function of frequency. The lighter line to the right shows the natural crystal response. The heavier line to the left shows the response after the crystal has been mounted in the camera and stressed to its optimal value. A series of filters matches the band-pass of the instrument to the atmospheric window. Figure 2 shows the combined band-pass filtering of the system.

A drawing of one of the stressing blocks is shown in Figure 3(a). The crystals are mounted in the integrating cavities on the front of the stressing block (on the left of Figure 3(a)) and a stressing rod is pushed up into the rear of the block (on the right of Figure 3(a)) using a stressing screw. This in turn operates a lever which applies the stress downwards through the line of crystals by means of further stressing rods.

There are three stressing blocks. The centre block holds three crystals and the two side blocks hold two crystals each, such that when the three blocks are fixed together, as in Figure 3(b), the crystals make a hexagonal arrangement. The crystal integrating cavities are coupled to the telescope by individual feed-horns, as shown in Figure 3(b), with a resolution of 14 arcsec, as for the SCUBA $850\text{-}\mu\text{m}$ array (Holland et al., 1999). The THUMPER focal plane array can also be adjusted to match the SCUBA $450\text{-}\mu\text{m}$ array if desired, although this mode was not used on this occasion. We

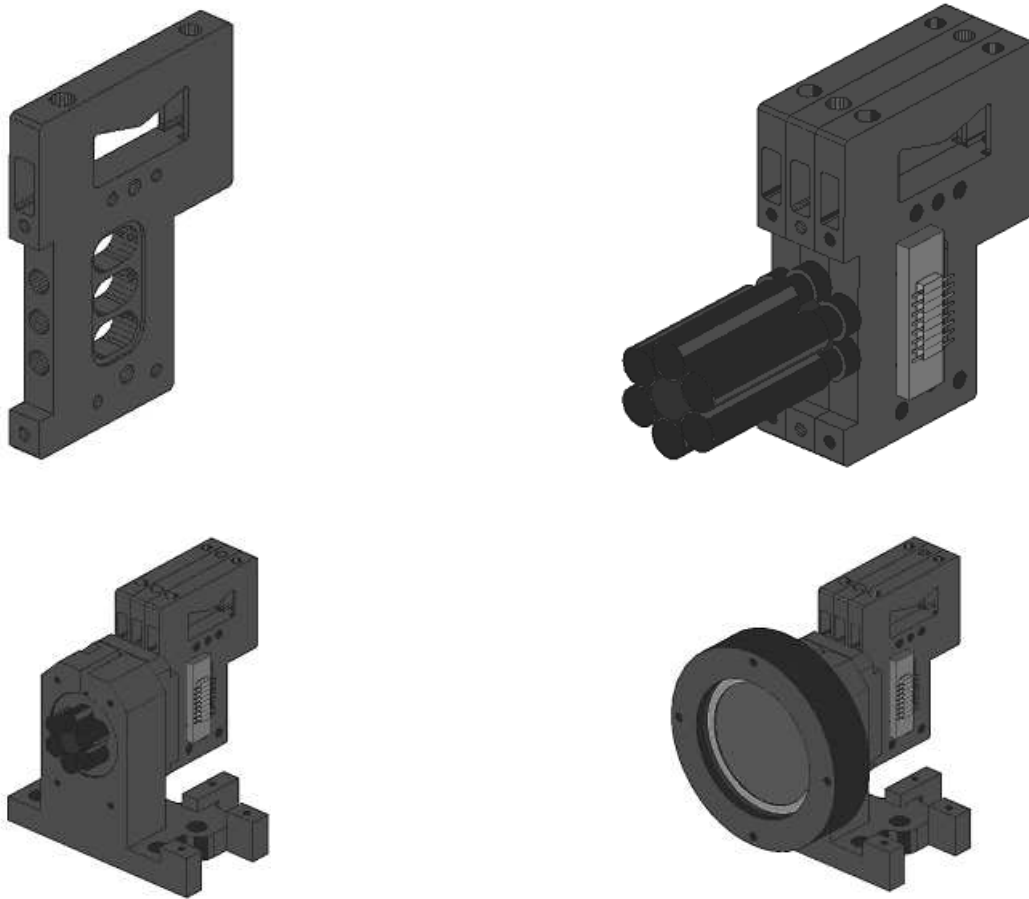


Figure 3. The THUMPER focal plane array: (a: top left) a stressing block in which the crystals are mounted; (b: top right) the three stressing blocks fixed together to form the focal plane array, with feed-horns on the front of the detectors; (c: lower left) the focal plane array mounted on its stand; (d: lower right) the complete array and mount with the filter stack mounted on the front.

chose not to make the feed-horns diffraction-limited on the telescope because the dish surface accuracy is too low to provide a significant fraction of the total incident power in a diffraction-limited beam at this wavelength.

The focal plane array is mounted in a stand as shown in Figure 3(c) and the filter stack attached to the front of the array as seen in Figure 3(d). The whole array is cooled to liquid Helium temperature (3.7 K at JCMT) in a long hold-time cryostat, built by Queen Mary College Instruments (now based at Cardiff University) and Thomas Keating Ltd. The system detector quantum efficiency (DQE) was measured in the laboratory. Calculations were performed based upon the optical set-up of the instrument at the telescope, including estimates of the dish surface accuracy. Incorporating all of these factors we estimated before going to the telescope that the noise equivalent flux density (NEFD) of the JCMT-THUMPER arrangement should be $\sim 50\text{--}70$ Jy (1σ 1s – Walker 2004).

3 OBSERVATIONS

The cryostat was mounted on the right Nasmyth platform of the JCMT. Two lenses, made of high-density polyethylene, were used to bring the beam from the telescope to the $f/5.75$ focus required by THUMPER (Walker et al. 2003).

The instrument was commissioned during Director’s Discretionary Time in two 4-night observing runs on 2005 March 20-23, and 2005 April 6-9. Optical alignment and instrument setup were carried out prior to this. Data acquisition was carried out via a stand-alone computer operating the LabVIEW software system (Laboratory Virtual Instrument Engineering Workbench). Only one of the scheduled nights was good enough for astronomical observations at this wavelength, 2005 April 9, when our observing was scheduled from 01.30 to 09.30 Hawaiian Standard Time (UT 11.30 to 19.30). Data from that night are presented in this paper.

4 THE 200-MICRON SKY

The 200- μm (1.5 THz) atmospheric window is much narrower in wavelength than the more commonly used sub-millimetre windows, and has much lower transmission. We modelled this window, along with neighbouring windows, using the Cardiff-developed software package FETCH (Araujo et al., 2001; Hayton et al., 2005). This is a fast, highly flexible line-by-line, layer-by-layer, radiative transfer model that uses the latest High-resolution Transmission (HITRAN) molecular spectroscopic database (2004 version) to calculate the atmospheric transmission as a function of frequency (Rothman et al., 2003; 2005). We found that the window

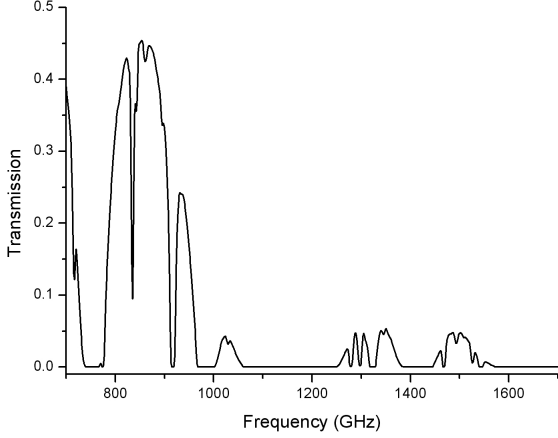


Figure 4. Plot of atmospheric transmission versus frequency as we have modelled, for 0.5mm PWV. Note the more frequently used sub-millimetre window at 850 GHz ($350 \mu\text{m}$). The 1.5-THz window is beginning to open up in these conditions.

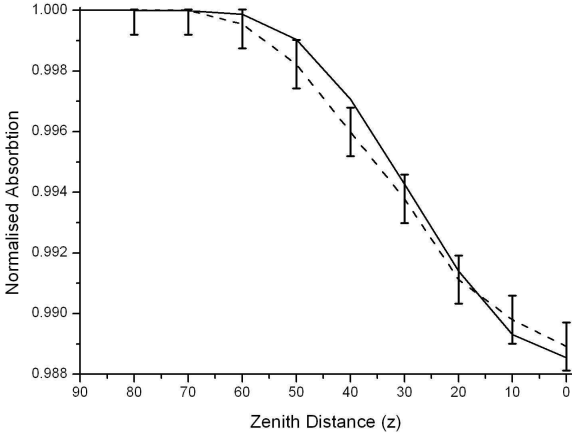


Figure 5. Plot of a typical set of sky-dip data. Normalised emission is plotted against zenith distance. The data-points are shown, along with estimated error-bars, joined by a dashed line. The solid line is a fit to the data used to obtain $\tau_{1.5\text{THz}}$. See text for details.

extends from 1428 to 1588 GHz ($189\text{--}210 \mu\text{m}$), with peak transmission at 1486 GHz ($202 \mu\text{m}$). The reason why the peak wavelength is not centred in the window is that there is an absorption line directly in the centre of the window.

Figure 4 shows the result of the detailed model calculations of the transmission across the whole of this part of the spectrum, assuming that the atmospheric precipitable water vapour (PWV) content is 0.5 mm. The more familiar window at 850 GHz ($350 \mu\text{m}$) can be seen, along with the small transmission window just opening at 1.5 THz ($200 \mu\text{m}$). The peak transmission is low, but nonetheless useable for part of the time. This calculation is consistent with the measurements of Paine et al. (2000), under better atmospheric conditions in Chajnantor, Chile – see their figure 3.

On the occasions when the sky was totally opaque we measured the relative responsivity of the seven channels by measuring the sky emission at zenith. This is essentially a flat, extended source, and allowed us to make a flat-field of our focal plane array. This remained remarkably constant,

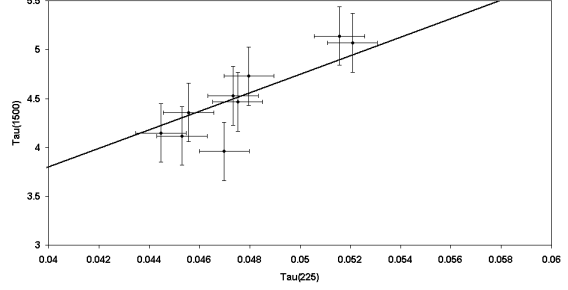


Figure 6. Plot of $\tau_{1.5\text{THz}}$ versus $\tau_{225\text{GHz}}$. The data are shown as crosses. The solid line is a least-squares fit to the data. The best fit straight line that we find is $\tau_{1.5\text{THz}} = (95 \pm 10) \times \tau_{225\text{GHz}}$.

and was also consistent with our sensitivity measurements made in the laboratory.

During the times when we could carry out astronomical observations we calibrated the sky transmission using the method of sky-dipping. This entails measuring the sky emission at several positions between zenith and horizon, and modelling the profile as a function of zenith distance, z . The emission is predicted to have the form $(1 - e^{-\tau \sec z})$, and hence a fitting routine can be used to calculate the optical depth, τ .

Figure 5 shows the result of a typical sky-dip. On the x-axis is plotted zenith distance z from 90° to 0° , while the y-axis gives the emission measured from the sky at a given value of z , normalised to the peak emission at 90° . The data-points with error-bars are shown connected by a dashed line, while the solid line shows the model fit to the data for an optimised value of the optical depth, τ .

Throughout our observations, the JCMT water vapour monitor (WVM) measured the atmospheric opacity at 183 GHz and from this calculated the opacity at 225 GHz (for historical reasons) in the standard way in which it records these data (e.g. Archibald et al., 2002). The WVM operates via a pick-off mirror at the edge of the JCMT field of view. It updates its estimate of the 225-GHz opacity every 1.2 seconds. Consequently, at the time of each sky-dip we know the value of the 225-GHz opacity, so we can plot it against our measured 1.5-THz opacity.

Figure 6 shows the resultant plot of $\tau_{1.5\text{THz}}$ versus $\tau_{225\text{GHz}}$. The data are shown as crosses. Our sky model calculations (see above) predict a linear relation between these two frequencies over the observed range of values. The solid line is the resulting least-squares fit to the data. The best fit straight line that we find is:

$$\tau_{1.5\text{THz}} = (95 \pm 10) \times \tau_{225\text{GHz}}.$$

This result is consistent with our model predictions and can also be compared with those obtained by previous workers. For example, Matsushita et al. (1999), found a relation of the form $\tau_{1.5\text{THz}} = (105 \pm 32) \times \tau_{225\text{GHz}}$ for the observing site at Pampa la Bola in Chile.

These latter authors used an FTS to measure the atmospheric opacity across the different wavebands, whereas we are comparing our data to WVM data. Nevertheless, recent work shows that provided all relevant effects are taken into consideration, the results from FTS and WVM measurements generally agree well (Pardo et al. 2004). Hence

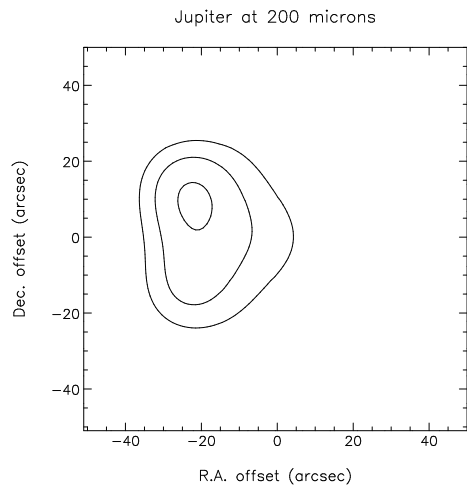


Figure 7. First-light astronomical image taken with THUMPER: A 200- μm isophotal contour map of Jupiter. The field of this image roughly corresponds to the size of the THUMPER array. The centre of the array is at (0,0). Contour levels are at 50, 70 & 90% of peak. The fact that the image appears slightly non-circular shows that part of the error-beam of the telescope may be affecting the data. The optical alignment is also slightly offset.

our result is fully consistent with previous work. Therefore we can use this relation to calibrate our subsequent measurements.

5 PLANET MAPS

5.1 Jupiter

The first astronomical object we imaged was Jupiter. Figure 7 shows our 200- μm map of Jupiter. It was constructed from two consecutive maps of Jupiter, taken immediately one after the other, over the airmass range 1.25 to 1.27. The two maps both show the same structure, and so they were co-added to increase the signal-to-noise ratio. We note that the source is not exactly centred in the image, being misaligned by ~ 30 arcsec. The telescope absolute pointing accuracy (based on measurements made with other instruments) at this time was ≤ 3 arcsec. This implies that our system alignment was not perfect. This is not surprising given that this was the first time that THUMPER had been mounted on JCMT and this was the first-light astronomical image.

The flux density of Jupiter at this wavelength can be predicted from planetary modelling (Griffin et al., 1986; Orton et al., 1986; Griffin & Orton 1993). Based on this, we expect the peak flux density of Jupiter to be 34 kJy/beam. During the observations the measured value of $\tau_{225\text{GHz}}$ was 0.0625. Using our relation above, between 1.5THz and 225GHz, this corresponds to a value of $\tau_{1.5\text{THz}}$ of ~ 5.95 .

Therefore the observed flux density at the telescope is predicted to be 21 Jy/beam. The total integration time per point of the two co-added maps was 100 seconds. The peak was detected at a level of $\sim 3.3 \sigma$. Therefore we calculate from the Jupiter data that the noise equivalent flux density (NEFD) of the JCMT-THUMPER combination is $\sim 63 \pm 10$ Jy (1σ 1s).

We note that our detection is not at the $5\text{-}\sigma$ level. How-

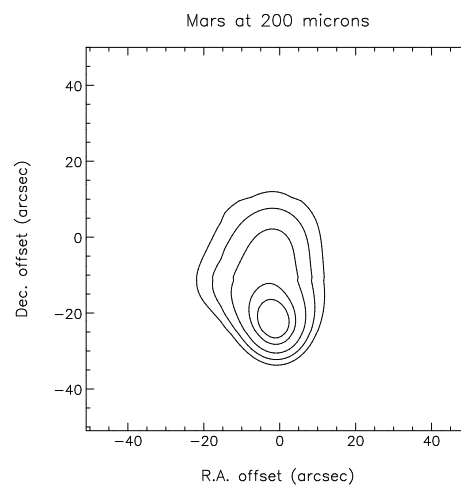


Figure 8. A 200- μm isophotal contour map of Mars taken by THUMPER on JCMT. The contour levels are at 50, 60, 70, 80 & 90% of peak. Once again the array centre is at (0,0). The alignment is improved in R.A. The extension to the north is the telescope error beam, which probably also extends to the south, although this was not mapped.

ever, we believe it is a real detection for a number of reasons: the source was seen in several pixels simultaneously; the structure in the two maps that we took was the same; the source appeared in the same place in both maps; and the NEFD we calculate from the measurements is consistent with that predicted from laboratory measurements of the detector system. In re-gridding the map onto an RA-Dec grid as shown in Figure 7 some smoothing naturally occurred, as a pixel scale of 5 arcsec was adopted.

The full-width at half-maximum (FWHM) of Jupiter in our map is $\sim 46 \times 38 (\pm 8)$ arcsec. At the time of the observations, the diameter of Jupiter was 42 arcsec. When convolved with our 14-arcsec beam, this becomes 44.2 arcsec. Hence our observations are consistent with this. However, the non-circularity visible in the map shows that we are also detecting part of the telescope error beam, which is predicted to be significant at this wavelength. We could not trace the error beam further in these data due to their low signal-to-noise ratio.

It is also possible that if we did not have the instrument exactly in focus then this would also contribute to the apparent non-circularity of the beam. We focussed the instrument using our model of the telescope and our calculation of the optimal focal position. However, we did not have time to check the focus on-source before Jupiter began to set.

5.2 Mars

Later in the night we imaged Mars as it was rising, from airmass 1.30 to 1.29. Figure 8 shows our map of Mars. Once again the source is not centred, although we have managed to improve the alignment in R.A. at least. The flux density of Mars at this wavelength can be predicted from planetary modelling in the same way as that of Jupiter quoted above (Griffin et al., 1986; Orton et al., 1986; Griffin & Orton 1993). Based on this, we expect the peak flux density of Mars to be 8.1 kJy/beam. During the observations the measured value of $\tau_{225\text{GHz}}$ was 0.0455. Using our relation

above, between 1.5 THz and 225 GHz, this corresponds to a value of $\tau_{1.5\text{THz}}$ of ~ 4.32 .

Therefore the observed flux density at the telescope is estimated to be 30 Jy/beam. The integration time per point of the map was 50 seconds. The peak was detected at a level of $\sim 3.2\sigma$. Therefore we calculate from the Mars data that the noise equivalent flux density (NEFD) of the JCMT-THUMPER combination is $\sim 66 \pm 10$ Jy (1σ 1s).

We note once again that our detection is not at the 5σ level. However, we believe it is also a real detection for similar reasons to those quoted above: the source was seen in several pixels simultaneously; and the NEFD we calculate from the measurements is consistent with that predicted from laboratory measurements of the detector system and with that seen in the Jupiter data.

The map of Mars shows a slightly different morphology from that of Jupiter. The map shows some evidence that the brightest region is more centrally peaked, and that this central peak sits on an extended plateau. Conversely, Jupiter is better fitted by a single gaussian. For Mars the centrally peaked core is of order ~ 15 arcsec across, with a more extended lobe to the north. The core is consistent with the FWHM that would be expected from Mars, since at the time of the observation the diameter of Mars was 6 arcsec. When convolved with our beam this produces a gaussian with FWHM 15.2 arcsec, consistent with the image in Figure 8.

The extended emission to the north is most likely to be the error-beam of the telescope. The level of the extended error-lobe is roughly two-thirds of the magnitude of the main beam. This may also extend to the south and south-east, but our map does not extend far enough in these directions to say. Once again the instrument focus may be adding to the problem. By the time we repeated the map the shift was coming to an end and the sun had risen. Consequently, the conditions worsened (the sky noise level increased) and we did not detect Mars again in day-time. Our mean NEFD measured on the planets is therefore $\sim 65 \pm 10$ Jy (1σ 1s).

6 THE SUN

Once the Sun had risen we pointed the telescope at the Sun, when it was in the airmass range 1.44 to 1.43, and detected it clearly in all channels, at high levels of signal-to-noise ratio of up to 560σ . Obviously, we did not map the full extent of the Sun, but rather used it as a bright, uniform, extended black-body source, and chopped across the limb of the Sun. We estimate that the emission from the Sun is ~ 1.1 MJy/beam. It was at ~ 1.4 airmasses during our observation, and $\tau_{225\text{GHz}}$ was 0.047. We used 5-second integrations, so we estimate our NEFD on the Sun to be ~ 9 Jy (1σ 1s).

This is a factor of ~ 7 better than our NEFD estimated from the essentially point-like planet Mars. This implies that only roughly one-seventh ($\sim 15\%$) of the total power incident upon the JCMT dish at $200\mu\text{m}$ is focussed into a 14-arcsec central beam. We had predicted that, due to the surface inaccuracies of the JCMT dish (which was not designed to operate at this high a frequency), there would be significant power in the side-lobes.

The measurement of the surface accuracy of the dish which is closest in time to our observations was taken on

2005 February 13, at which time the dish surface accuracy was found to be $23.8\mu\text{m}$ (Wouterloot 2005). Using the standard calculation of Ruze efficiency we estimate that a dish of this accuracy would concentrate $\sim 11\%$ of the total power into a 14-arcsec beam. This is consistent with the $\sim 15\%$ we estimate here based on the ratio of NEFDs measured on Mars and the Sun. Hence we see that all of our observations are self-consistent.

7 CONCLUSIONS

We have successfully commissioned the THUMPER camera at JCMT. We have demonstrated that $200\mu\text{m}$ astronomy is possible from the ground. We have taken the first ground-based images of Jupiter and Mars at this wavelength. We have calibrated the $200\mu\text{m}$ sky, and found a relation between opacities of $\tau_{1.5\text{THz}} = (95 \pm 10) \times \tau_{225\text{GHz}}$. This is consistent with previous measurements, and also with our modelling of atmospheric transmission across this section of the electro-magnetic spectrum. We estimate the NEFD of the JCMT-THUMPER system is ~ 65 Jy (1σ 1s). We find that the error beam of JCMT is substantial at this wavelength, as predicted, with only $\sim 15\%$ of the power appearing in the central 14 arcsec. We note that a telescope with a greater surface accuracy would improve upon this number, and that other observing sites in even higher or drier locations may provide a larger number of useable observing nights per year. Based on its current NEFD, it seems that THUMPER could be used to study bright, high-mass, star-forming regions at higher angular resolution than has been previously possible at this wavelength.

ACKNOWLEDGMENTS

The THUMPER Team would like to acknowledge the assistance of the staff of the JCMT throughout the planning and commissioning of THUMPER. The JCMT is operated by the Joint Astronomy Centre, Hawaii, on behalf of the UK Particle Physics and Astronomy Research Council (PPARC), the Netherlands Organization for Scientific Research (NWO), and the Canadian National Research Council (NRC). PPARC are gratefully acknowledged for grant funding to build THUMPER.

REFERENCES

- Araujo H. M., Walker R. J., Rinehart S. A., Griffin M. J., Ade P. A. R., 2001, *Int. J. IR & mm waves*, 22, 965
- Archibald E. N., Jenness T., Holland W. S., Coulson I. M., Jessop N. E., Stevens J. A., Robson E. I., Tilanus R. P. J., Duncan W. D., Lightfoot J. F., 2002, *MNRAS*, 336, 1
- Beichman C. A., Neugebauer G., Habing H. J., Clegg P. E., Chester T. J., eds, 1988, *Infrared Astronomical Satellite Catalogs and Atlases Explanatory Supplement*, NASA RP-1190, Vol. 1. US Government Printing Office, Washington DC
- Cameron R. M., Bader M., Mobley R. E., 1971, *Applied Optics*, 10, 2001
- Chamberlin R. A., Martin R., Martin C. L., Stark A. A., 2003, in: Phillips T. G., Zmuidzinas J. (eds.), 'Millimeter and Submillimeter Detectors for Astronomy', SPIE, 4855, 609, Bellingham, Washington State, USA

- Evans R., Ward-Thompson D., Leeks S. J., Walker R. J., Ade P. A. R., Gear W. K., Griffin M. J., Gannaway F., Kiernan B., Rinehart S. A., Araujo H., 2005, in: Wolfe J., Davidson J., eds., ‘Far-IR, sub-mm & mm detector technology’, in press
- Gerecht E., Yngvesson S., Nicholson J., Zhuang Y., Rodriguez-Morales F., Zhao X., Gu D., Zannoni R., Coulombe M., Dickinson J., Goyette T., Waldman J., Groppi C., Hedden A., Golish D., Walker C., Stark A., Martin C., Lane A., 2003, in: Phillips T. G., Zmuidzinas J. (eds.), ‘Millimeter and Submillimeter Detectors for Astronomy’, SPIE, 4855, 574, Bellingham, Washington State, USA
- Griffin M. J., Ade P. A. R., Orton G. S., Robson E. I., Gear W. K., Nolt I. G., Radostitz J. V., 1986, *Icarus*, 65, 244
- Griffin M. J., Orton G. S., 1993, *Icarus*, 105, 537
- Harvey P. M., 1979, *PASP*, 91, 143
- Hayton D., Watkin S. L., Ade P. A. R., 2005, in prep
- Holland W. S., Robson E. I., Gear W. K., Cunningham C. R., Lightfoot J. F., Jenness T., Ivison R. J., Stevens J. A., Ade P. A. R., Griffin M. J., Duncan W. D., Murphy J. A., Naylor D. A., 1999, *MNRAS*, 303, 659
- Kessler M. F., et al., 1996, *A&A*, 315, L27
- Matsuo H., Sakamoto A., Matsushita S., 1998, *PASJ*, 50, 359
- Matsushita S., Matsuo H., Pardo J. R., Radford S. J. E., 1999, *PASJ*, 51, 603
- Orton G. S., Griffin M. J., Ade P. A. R., Nolt I. G., Radostitz J. V., Robson E. I., Gear W. K., 1986, *Icarus*, 67, 289
- Paine S., Blundell R., Papa D. C., Barrett J. W., Radford S. J. E., 2000, *PASP*, 112, 108
- Pardo J. R., Wiedner M. C., Serabyn E., Wilson C. D., Cunningham C., Hills R. E., Cernicharo J., 2004, *ApJS*, 153, 363
- Rothman L. S., et al., 2003, *J. Quant. Spec. Rad. Tran.*, 82, 5
- Rothman L. S., et al., 2005, *J. Quant. Spec. Rad. Tran.*, in press
- Serabyn E., Weisstein E. W., 1996, *Applied Optics*, 37, 2185
- Serabyn E., Weisstein E. W., Lis D. C., Pardo J. R., 1998, *Applied Optics*, 37, 2185
- Ward-Thompson D., Evans R., Leeks S. J., Walker R. J., Ade P. A. R., Griffin M. J., Gear W. K., 2002, *JCMT Newsletter*, 18
- Walker R. J., Ward-Thompson D., Evans R., Leeks S. J., Ade P. A. R., Gear W. K., Griffin M. J., Gannaway F., Kiernan B., Rinehart S. A., Araujo H., 2003, in: Phillips T. G., Zmuidzinas J., eds., ‘Millimeter and submillimeter detectors for astronomy’, *Proc. SPIE*, 4855, 563
- Walker R. J., 2004, PhD Thesis, Cardiff University
- Werner M. W., et al., 2004, *ApJS*, 154, 1
- Wouterloot J., 2005, ‘The JCMT dish surface’ web-page, url: www.jach.hawaii.edu/JCMT/telescope/surface